MDPI

Article

Microstructures and Mechanical Properties of Ductile Cast Iron with Different Crystallizer Inner Diameters

Jiaojiao Bai [1,2], **Haifeng Xu** [2], **Yuhui Wang** [3], **Xingpin Chen** [1,*], **Xiaodan Zhang** [4,*], **Wenquan Cao** [2,*] **and Yang Xu** [5]

[1] College of Materials Science and Engineering, Chongqing University, Chongqing 400044, China; m18798011462@163.com
[2] Central Iron and Steel Research Institute (CISRI), Beijing 100081, China; xuhaifeng228@163.com
[3] National Engineering Research Center for Equipment and Technology of Cold Strip Rolling, Yanshan University, Qinhuangdao 066004, China; yhwang@ysu.edu.cn
[4] Section of Manufacturing Engineering, Department of Mechanical Engineering, Technical University of Denmark, 2800 Kongens Lyngby, Denmark
[5] College of Materials Science and Engineering, Xi'an University of Technology, Xi'an 710000, China; jhlz_xy@sina.com
[*] Correspondence: xpchen@cqu.edu.cn (X.C.); xzha@mek.dtu.dk (X.Z.); caowenquan@nercast.com (W.C.)

Abstract: Five types of ductile cast irons (DCIs) were fabricated by crystallizers with different inner diameters, as well as five different austempered ductile cast irons (ADIs) after the same isothermal quenching process. The effects of amount, diameter, and morphology of graphite on the mechanical properties of DCI and ADI and the effect of the original as-cast microstructure on the microstructure after austempering were studied. The microstructures were characterized by optical microscopy, scanning electron microscopy, and X-ray diffraction. Their mechanical properties were examined by tensile, U-shaped impact, and hardness tests. As the diameter of the crystallizer increases from 60 mm to 150 mm, the diameter of the nodular graphite increases from ~10 to ~50 μm, and the nodularity rate decreases from 100 to 70%. The average ultimate tensile strength increases from ~500 MPa in the as-cast state to 1100 MPa in the austempered state and the hardness increases from ~180 HB to 400 HB. The elongation in cast state decreases from 11 to 4.6% and the elongation in ADI state decreases from 7 to 4.5%. Through the research in this paper, it can be seen that ADIs with different matrix microstructures can be obtained from different original as-cast microstructures through the same isothermal quenching process, and different casting crystallizers can be selected according to different performance requirements, which can reduce the nitrite pollution and reduce cost.

Keywords: austempered ductile cast iron; nodular graphite; cooling rate; microstructure; mechanical properties

1. Introduction

The cast iron industry has developed rapidly and has played an important role in iron and steel research [1]. Microstructural characteristics of cast iron, such as the graphite shape and distribution, and the metal matrix microstructure, depend on the chemical composition, the casting process, and the cooling condition [2]. The nodularity rate varies in a cast component because of variations in the crystallizer inner diameter and heat dissipation in different regions of the crystallizer [3]. For ductile iron with nodular graphite particles, the overall graphite volume, area fraction of the nodular graphite (nodularity), number of nodules per unit area (nodule number), nodular graphite diameter and matrix microstructure are influenced by the solidification condition and addition of alloying elements [4]. The microstructural characteristics, such as the amount of ferrite/pearlite, the nodularity rate, the nodular size and morphology, affect the mechanical properties of ductile iron significantly [5–8].

Although the original as-cast ductile iron has a good toughness, its strength is too low to meet production requirements of many components. Austempered ductile cast iron (ADI) has emerged as an important engineering material in recent years. This material has many attractive properties, such as high strength and good wear resistance, superior fatigue properties, and high fracture toughness [9–11]. As a result, ADI is considered a very promising engineering material.

The excellent properties of ADI are related to its unique microstructure. During austempering, ductile iron undergoes a two-stage phase transformation. In the first stage, austenite (γ) decomposes to ferrite (α) and high carbon austenite (γ_{hc}) because of the high silicon content of ductile iron, which suppresses carbide formation. As the carbon-rich austenite is very stable, the combination of ferrite and residual austenite is the most desirable microstructure and gives ADI excellent properties. If ductile cast iron is held at this temperature for a prolonged period, a second reaction occurs. During the second stage, γ_{hc} can decompose to ferrite (α) and carbide (ε) [5]. Because this structure contains ε carbide, which makes the material brittle, this reaction must be avoided. The optimum austempering period is the duration between the end of the first reaction and the beginning of the second reaction, which is sometimes referred to as the "processing window". The Si content in ductile cast iron is high, which can promote the separate nucleation of ferrite in austenite, inhibit the formation of cementite, and accelerate the diffusion of carbon atoms in austenite. The toughness and stability of austenite increase significantly with an increase of carbon content in austenite. The formation of acicular ferrite without carbide precipitation and a significant increase of carbon content of austenite are important features of this austempered transition. High-carbon austenite and acicular ferrite have an excellent toughness, and the matrix does not contain brittle phase cementite.

The exact morphology of the ferrite phase and the relative amounts of ferrite and austenite can be controlled by adjusting the austempering temperature and time, which will further determine the mechanical properties of the ADI [7,12–15]. When ADI is austempered at lower temperatures, different bainite ferrite morphologies, volume fractions of high-carbon austenite and carbon contents in austenite can be obtained [16]. When the ADI is austempered at higher temperatures, an ausferritic microstructure is produced, which is a combination of carbide-free ferrite and austenite. The ferrite becomes feathery (coarse) and it has a lower yield strength, which decreases the yield strength of the ADI [17,18]. In addition, different morphologies of graphite also have a great influence on the mechanical properties of the material. T. Borsato [19] studied that degenerated graphite particles (spiky graphite) increase the notch effect of crack nucleation, thereby reducing the fatigue strength of the material. Y. Liu [8] has researched that the tensile strength of compacted graphite iron with low nodularity rate is lower than that of ductile cast iron with nodularity rate greater than 95%. Because the stress concentration is easily formed at the tip of the vermicular graphite, cracks are easily formed here. The ADI has good mechanical properties, and its strength is one to two times higher than the ductile iron. However, isothermal quenching requires a salt bath treatment and a large initial investment in the production equipment, yields serious nitrite pollution, and has a low productivity, high energy consumption, and a high cost.

This work focuses on the effect of cooling rates controlled by the different crystallizer inner diameter on microstructure and properties of the of cast iron and the ADI. After the same austempering process, the effect of graphite quantity and size on the properties of cast iron and ADI and the effect of the original microstructure are investigated. The number of graphite nodules, the nodular graphite size, the number and morphology of the ferrite plates, and the high carbon austenite determine the final properties of the ADI castings. For this purpose, five kinds of ductile cast irons are fabricated by melting and casting with different crystallizer inner diameters. A microstructural investigation and the mechanical testing of the ductile iron and ADI are performed.

2. Materials and Methods

2.1. Experimental Materials

The material was cast via the vertical continuous casting of ductile iron profiles by using the bread pig iron, the scrap steel, and the cast-iron alloy. Compared with other casting methods, the microstructure obtained by vertical continuous casting is more uniform. During vertical continuous casting of hollow profiles, the distribution of liquid and solid phases in the longitudinal and transverse sections of the crystallizer occurs as shown in Figure 1. The figure on the left in Figure 1 is a schematic diagram of the convection of molten iron in the crystallizer, and the figure on the right is a schematic diagram of the centripetal solidification of the crystallizer. The phase transformation and solidification in the crystallizer is similar when the solid bar is continuously cast vertically.
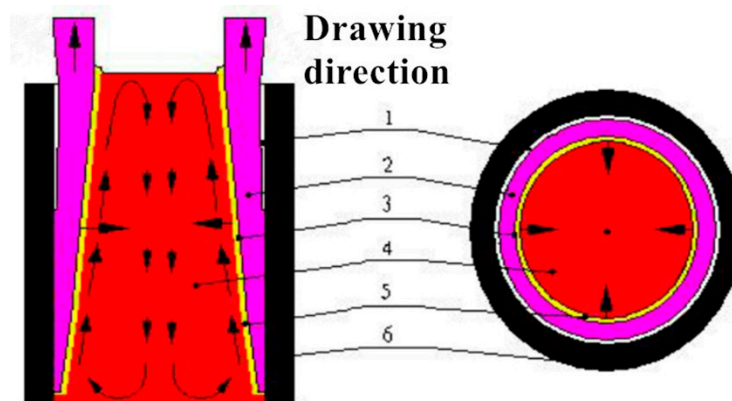
Figure 1. Convection of molten iron in the crystallizer (**left**) and the centripetal solidification in the crystallizer (**right**). 1—air gap, 2—solidified shell, 3—liquid/solid interface propelled from outside to inside, 4—molten iron, 5—high temperature molten iron layer formed by latent heat of crystallization, 6—graphite sleeve.

The high temperature molten iron layer caused by the latent heat of phase change is represented in the yellow section in Figure 1. This layer of high temperature molten iron caused the upper and lower convection of the molten iron, as represented by the arrow in the cavity in Figure 1. The effects of this convection are as follows:

(a) Under the action of convection stirring, the composition of the molten iron was consistent throughout the crystallizer, so that the composition on the cross section of the cast pipe or cast rod was uniform inside and outside without segregation. The segregation of alloying elements is detrimental to their properties [20].

(b) The liquid–solid interface is a three-dimensional tapered tube shape. Under the action of the free energy of phase change provided by cooling, crystal nuclei are continuously generated on the interface, which then grow up, thickening the tube wall. However, under the effect of the convective erosion of molten iron, a part of the initial crystal nuclei will float up and adhere to the upper tube wall. The higher the tube wall, the more floating crystal nuclei can be obtained, which is equivalent to increasing the nucleation rate, making the deep part of the tube wall or the core of the bar finer. Offsetting the slower cooling rate of the core of the profile causes coarse microstructures.

(c) The as-cast structure of the vertical continuous casting profile is dendritic on the outside, and equiaxed crystals begin to appear at about 15 mm from the outside wall. However, in the subsequent annealing and quenching process, multiple phase transformations and recrystallization occur, making the dendrites become equiaxed crystals that have been greatly refined, and the internal and external microstructures tend to be similar and consistent.

The hot metal components were configured according to mass percentage: C: 3.4–3.7%, Si: 1.5–1.7%, Mn: 0.3–0.5%, S $\leq$ 0.05%, P $\leq$ 0.05%, Fe and other impurities formed the balance. After the molten iron was melted in an intermediate frequency induction furnace nodulizer, the 75 FeSi inoculant was added into the melt. The temperature of the molten iron that emerged from the furnace during casting was 1480 °C, and the starting solidification temperature was ~1250–1300 °C. Because ductile iron is a multi-element Fe-C-Si alloy, the cooling rate of continuous casting is very fast, so its crystallization process occurs within a certain temperature range, rather than as a certain critical point temperature, as indicated on the two-dimensional equilibrium phase diagram. Crystallizers with diameters of 60, 75, 95, 120, and 150 mm were used. After incubation and nodularization, the final material composition was determined by infrared absorption method. The chemical compositions of samples were C 3.51, Si 2.8, Mn 0.32, S 0.0085, P 0.023, and Fe balance (wt.%).

Castings with different crystallizer inner diameters in the as-cast condition were marked as AC 60, AC 75, AC 95, AC 120, and AC 150, respectively. After fabrication, castings from the core of the original rods were cut into 60-mm-thick cylinders, which were austenitized at 900 °C for 2 h, then quenched into a salt bath (that contained 50% KNO_3 + 50% $NaNO_3$) at 250 °C and kept for 2 h. ADI samples were marked with different crystallizer inner diameters as ADI 60, ADI 75, ADI 95, ADI 120, and ADI 150, respectively.

2.2. Mechanical Testing

Tensile tests were carried out on a servo-hydraulic MTS test machine according to the standard ASTM E8M [21], with a gauge length of 30 mm. Three samples were tested under each heat-treated condition and the average values were reported. The tensile properties, including the tensile strength σ_b (MPa), yield strength $\sigma_{0.2}$ (MPa), reduction of area φ (%) and elongation δ (%), were calculated as the averages of three tests. Room temperature impact tests were carried out in a domestic JBN-300B pendulum chain-impact testing machine. The impact toughness was measured based on the average of five U-shaped Charpy impact tests according to the standard ASTM E23-2016b. Each was considered a valid K_{IC} value. Samples were cut into 55 mm × 10 mm × 10 mm. The hardness testing was carried out by using a Brinell Hardness tester at a 750-kg applied load and using a 5-mm diameter steel ball. The reported microhardness values are the average from five measurements.

2.3. Microstructural Observation

The microstructure was revealed by etching in 4% Nital for approximately 15 s. A Zeiss 40MAT microscope (Zeiss, Oberkochen, Germany)was used for low magnification observation of the microstructures in different states. A scanning electron microscope (SEM, FEI Quanta 650FEG, FEI, Hillsboro, OR, USA) was used to analyze the microstructures. Microstructural parameters, such as the nodular graphite number, the nodular graphite diameter, and the nodularity rate were evaluated according to the standard ASTM-A247-16a and measured by using Photoshop and Image-Pro Plus (IPP, Media Cybernetics, Rockville, MD, USA).

2.4. X-ray Diffraction Analysis

To quantify the volume fraction of residual austenite (V_γ) and the carbon content of austenite (C_γ) in the alloys, the samples were analyzed by the X-ray diffractometry (XRD). A D8 ADVANCE X-ray diffractometer with a Cu target, a tube current of 40 mA, a tube voltage of 35 kV, and a Lynxeye XE detector were used. Samples were scanned over a 2θ range from 40° to 100° with a step size of 0.02°. The profiles were analyzed by using Jade 6 software (MDI, USA) to obtain the peak positions and integrated intensities of (200), (220), (311), and planes of FCC austenite and (110) and (211) planes of BCC ferrite. The V_γ was calculated quantitatively by using Jade 6.0. The volume fraction V_γ was determined by the direct comparison method by using the integrated intensities of the above planes.

Three samples were examined from each heat-treated condition and the data reported are the averages from these samples. The carbon content of the austenite was determined by the following formula:

$$a_\gamma = 0.3548 + 0.00441 C_\gamma \tag{1}$$

where a_γ is the lattice parameter of austenite in nanometers and C_γ is the carbon content of austenite [12].

3. Experimental Results

3.1. Influence of Crystallizer Diameter on Graphite Size

Figure 2 shows the unetched micrograph of the cast and ADI states of five cast specimens. IPP software was used to calculate the graphite in both states after removing impurities in the 100 magnification field of view. Table 1 shows the average nodular graphite diameter in the as-cast and ADI states. Each sample randomly selects five fields of view and takes the average. As the diameter of the crystallizer increases, the diameter of the nodular graphite gradually increases in both states. Because graphite is at a stable phase, under the same crystallizer diameter, the nodular graphite diameters in the two states are basically the same. Thus, the change of nodular graphite during the heat treatment process could be ignored. This provides a basis for studying the influence of matrix structure on the mechanical properties. The nodular graphite diameter increases gradually with an increase in crystallizer inner diameter.
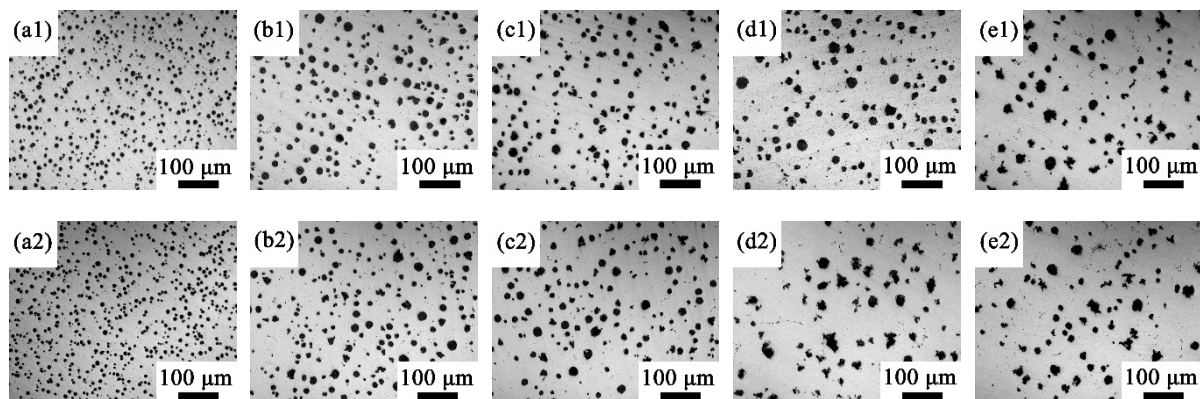
Figure 2. Microstructures of unetched as-cast specimens: (**a1**) AC 60, (**b1**) AC 75, (**c1**) AC 95, (**d1**) AC 120, (**e1**) AC 150 and austempered specimens (**a2**) ADI 60, (**b2**) DI 75, (**c2**) ADI 95, (**d2**) ADI 120, (**e2**) ADI 150.

Table 1. The nodular graphite diameter in cast and ADI states.

The Nodular Diameter/μm	Crystallizer Diameter (mm)				
	60	**75**	**95**	**120**	**150**
Cast	10	20	26	28	45
ADI	12	17	24	27	50

Figure 3(a1,b1,c1,d1,e1) shows the distribution of nodular graphite in the specimens from crystallizers with different inner diameters. Different colors represent different nodular graphite diameters. The amount of numbered nodular graphite with different diameters are shown by histograms in Figure 3(a2,b2,c2,d2,e2). According to ASTM-A247-16a, five fields were selected randomly for each sample to number the microstructural parameters. The highest nodularity rate (100%) occurred for the ADI 60, and the graphite diameter class is 8. As the crystallizer inner diameter increases, the amount of nodular graphite

decreases but the nodular graphite diameter increases, the nodularity rate decreases and chunks of graphite appeared as shown in Figure 2(d1,e1) and Figure 2(d2,e2). The nodularity rate for the ADI 75 and ADI 95 was 90%, for ADI 120 the rate was 80%, and for ADI 150 the rate was 70%. Above a diameter of 60 mm, the nodular graphite diameter class in ADI 75 and ADI 95 was 7, and for ADI 120 and ADI 150, it was 6. The analysis showed that different crystallizer inner diameters affected the nodular graphite diameter class, nodule number, and graphite nodularity in the ductile cast iron. This effect was attributed to the higher cooling rate in thinner crystallizers, which increased the number of nucleation sites for graphite particles and thus increased the graphite particle number [3,6].
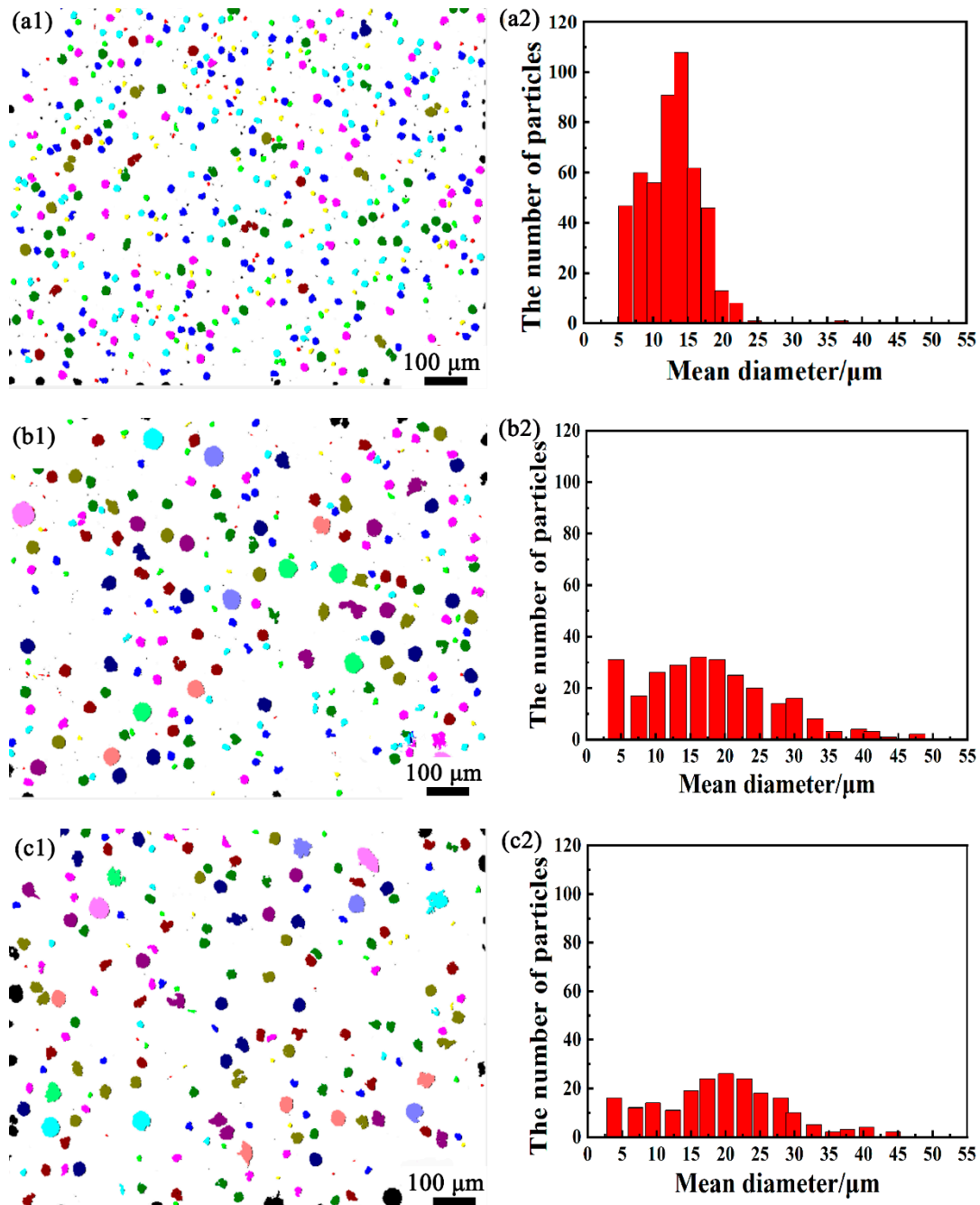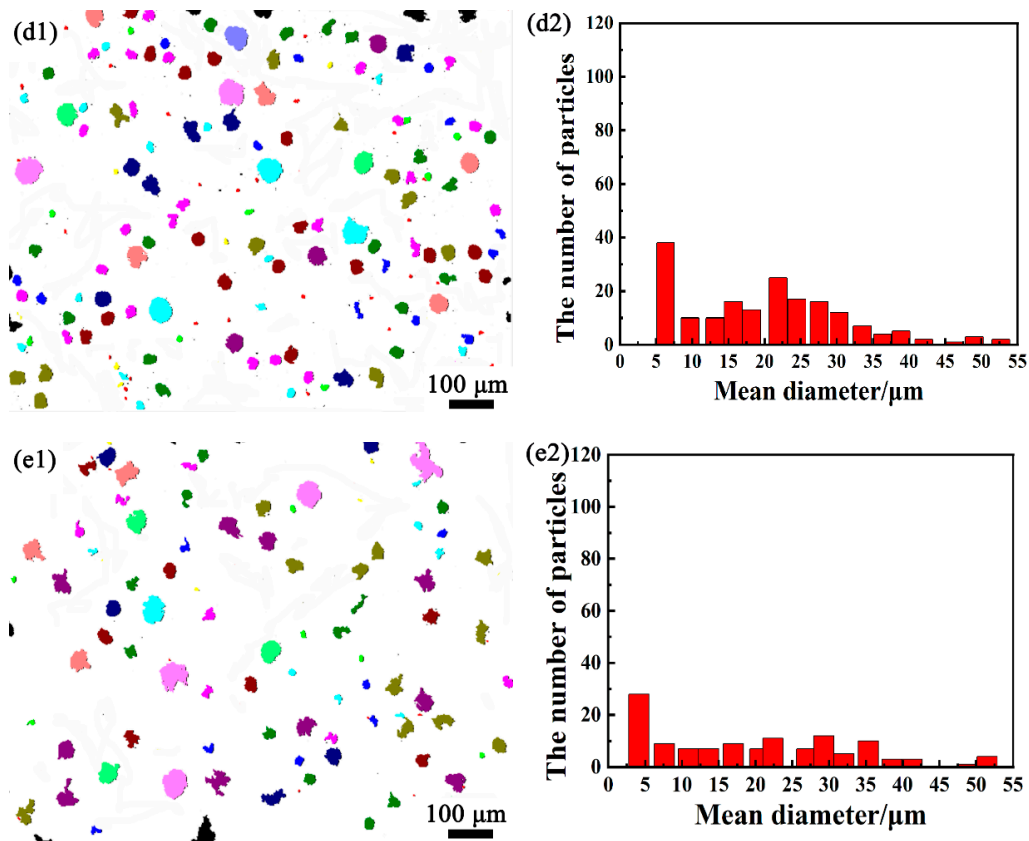

Figure 3. *Cont.*

Figure 3. Nodular graphite distribution and nodule number/mm^2 for different nodular graphite specimens: (**a1,a2**) ADI 60, (**b1,b2**) ADI 75, (**c1,c2**) ADI 95, (**d1,d2**) ADI 120, (**e1,e2**) ADI 150.

3.2. As-Cast State and ADI Matrix Microstructures

Figure 4 shows the metallographic and scanning micrographs of the etched as-cast sample. The left metallographic micrograph of Figure 4 shows that the as-cast structure was a typical "bulls'-eye" ferrite. The SEM micrograph analysis showed that the as-cast structure was composed of nodular graphite (black), ferrite (dark grey) around graphite and pearlite (light grey, lamellar) as shown on the right of Figure 4. The graphite size and the surrounding ferrite regions were increased by increasing the crystallizer inner diameter. This increase was attributed to the decrease in cooling rate with respect to the increase in crystallizer inner diameter. Lower cooling rates in the thicker crystallizer provided more time for carbon atoms to diffuse from the melt to graphite so that larger graphite particles, and consequently, coarser ferrite regions could be formed [22,23].
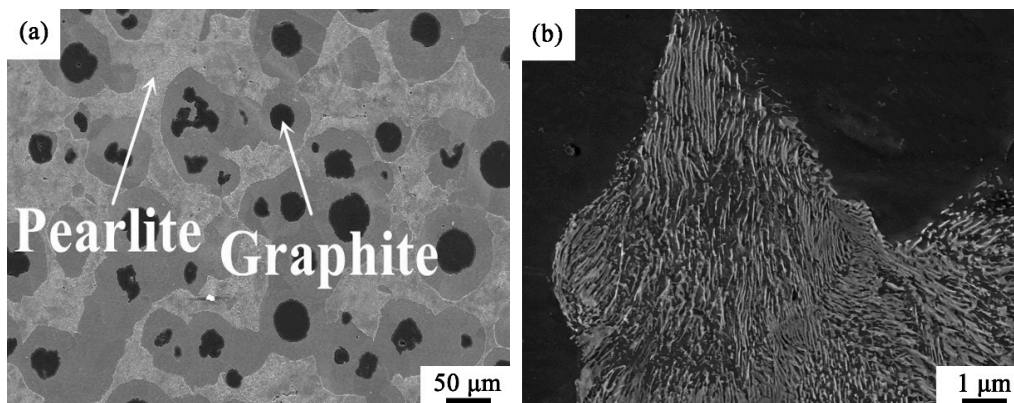
Figure 4. *Cont.*
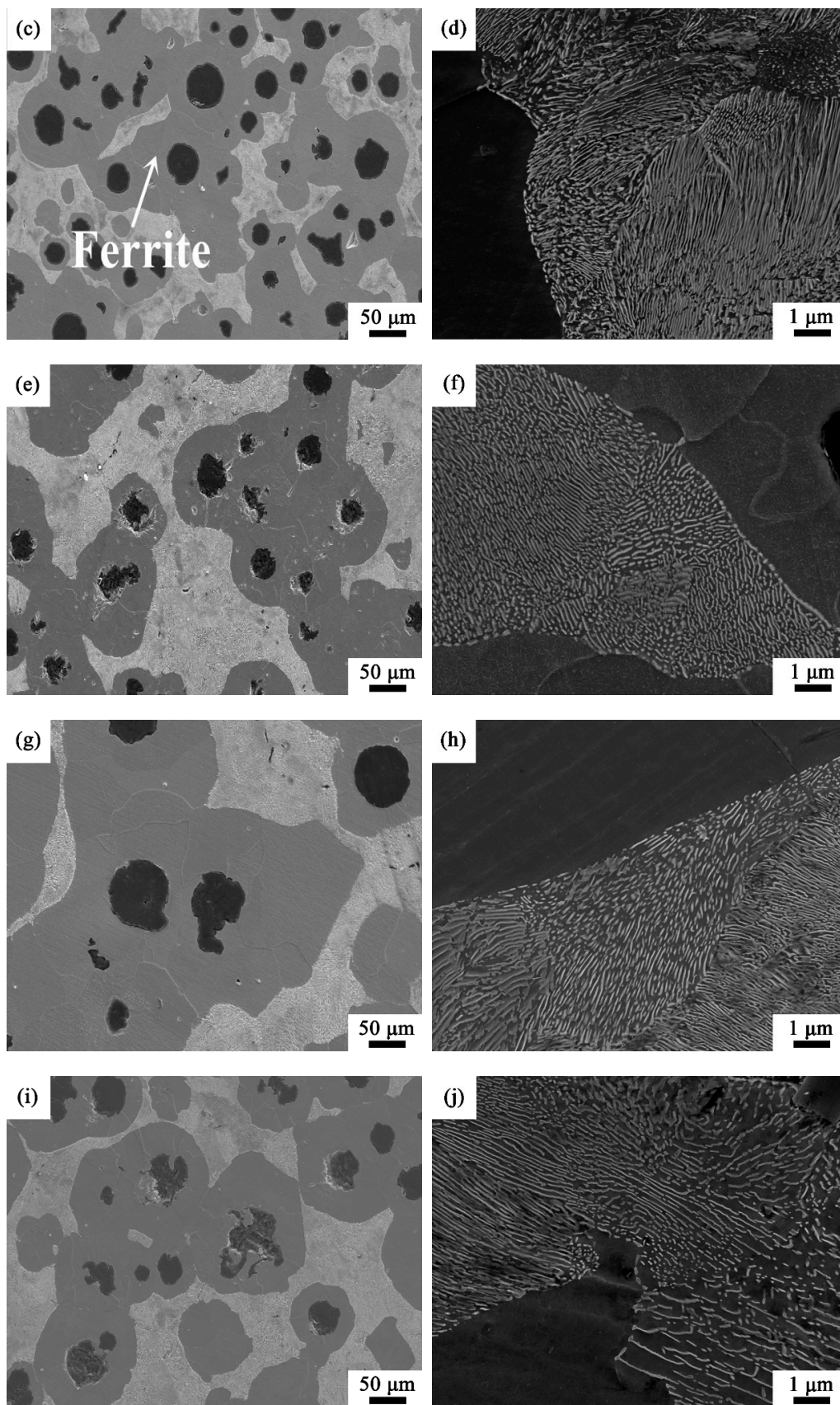
Figure 4. Microstructure of different as-cast specimens: (**a**,**b**) AC 60, (**c**,**d**) AC 75, (**e**,**f**) AC 95, (**g**,**h**) AC 120, (**i**,**j**) AC 150. Nodular graphite (black), ferrite (dark grey), and pearlite (light grey, lamellar).

Five pictures were selected, the area fraction of the different phases was determined, and the average was taken to yield the data in Table 2 for each as-cast specimen at the same magnification. The pearlite content first decreases and then increases with an increase of crystallizer inner diameter, and reaches a minimum at a diameter of 95 mm, and the ferrite content first increases and then decreases. Approximately the similar amount of nodular graphite exists in the first four specimens, while that in the AC 150 is the lowest.

Table 2. Area fractions of different phases in the as-cast samples (%).

| Phase (%)	Specimens				
	AC 60	**AC 75**	**AC 95**	**AC 120**	**AC 150**
Pearlite	29.9%	24.1%	17.6%	27.7%	33.4%
Ferrite	60.63%	65.47%	73.01%	62.38%	59.82%
Graphite	9.47%	10.43%	9.39%	9.92%	6.78%

The thinner crystallizer showed that a higher number of graphite particles resulted in a shorter distance between the particles and thus, a greater overlap between the ferrite regions that were formed around the graphite particles. With an increase in distance between the graphite particles, the ferrite no longer overlapped, and the ferrite area fraction increased. When the inner diameter of the crystallizer exceeded 95 mm, more time was provided for the carbon atoms to diffuse from the melt to graphite, so that larger graphite particles, and consequently, larger ferrite regions could form with a lower ferrite fraction. This trend was associated with a significant increase in distance between the graphite nodules (an increase in austenite diffusion paths for carbon), which resulted in a greater pearlite fraction in the areas between the graphite nodules (see Table 2).

Figure 5 shows the microstructures and XRD analysis of the five ADI samples after the same austempering treatment. ADI was composed of bainitic ferrite as dark needles (cross distribution) and white high-carbon residual austenite (γ_{hc}), as shown in Figure 5a. With an increase in crystallizer inner diameter, fewer bainitic ferrite needles, and coarse feathery bainite were observed, as shown in Figure 5d,e.

Table 3 shows the volume fractions of different phases with different inner diameters after austempering. The austenite carbon content was calculated and the average of the three peaks was calculated as C_γ. The C_γ in austenite differs for different crystallizer inner diameters. With an increase in diameter, the volume fraction of γ_{hc} (V_γ) content first increases and then decreases. The V_γ of the 75-mm-diameter sample reaches a maximum, whereas the fraction of bainitic ferrite showed an opposite trend. The C_γ of γ_{hc} differs for crystallizers with different inner diameters. With the increase in diameter, the C_γ in the austenite first increases, then decreases.

Table 3. Area fractions of different phases in ADI specimens (%).

Phase (%)	ADI Specimens				
	ADI 60	**ADI 75**	**ADI 95**	**ADI 120**	**ADI 150**
Austenite	13.3%	28.7%	26.8%	17.4%	23.6%
Graphite	9.54%	9.46%	9.31%	7.29%	6.78%
Bainitic ferrite	77.16%	61.84%	63.89%	75.31%	69.62%
C_γ	1.28%	1.30%	1.42%	1.8%	1.56%
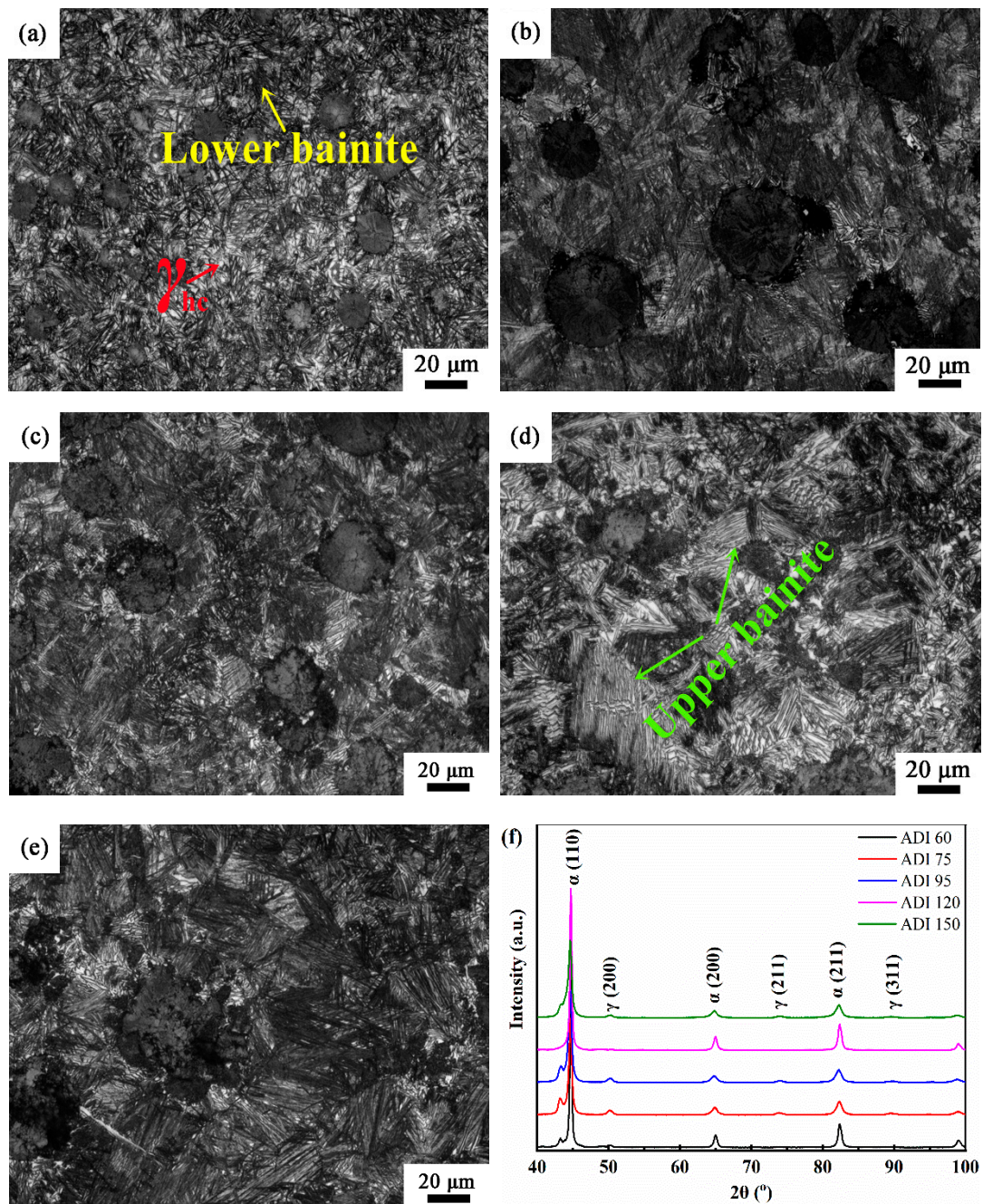
Figure 5. Microstructure of different ADI specimens: (**a**) ADI 60, (**b**) ADI 75, (**c**) ADI 95, (**d**) ADI 120, (**e**) ADI 150, (**f**) XRD analysis diagram. (Lower bainite (yellow arrow, needle-like), γ_{hc} (red arow), upper bainite (green arrow, feathery).

3.3. Mechanical Properties

The mechanical properties of as-cast and ADI state samples were determined by the Brinell hardness test, tensile experiments for the reduction of area φ (%), the elongation δ (%), tensile strength σ_b (MPa), yield strength $\sigma_{0.2}$ (MPa), and by the U-shaped notch impact test to calculate the impact energy. The results are shown in Figure 6.

As shown in Figure 6a, the ultimate tensile strength (σ_b) and yield strength ($\sigma_{0.2}$) of the ADI samples decrease initially, increase, and fluctuate with an increase in the crystallizer diameter, but little difference has been observed for AC 75–AC 150, which shows the same trend of hardness in Figure 6a. After the isothermal quenching, the average ultimate strength improved from 500 to 1100 MPa, and the average hardness increased by 140%.

Figure 6c,d shows the elongation, reduction of the area, and the impact energy of the crystallizer inner diameters 60–150 mm in the as-cast and ADI states. The trend of ADI 120 was different, which may be because of the dispersion nature of the graphite; big dispersion is expected. The final trend was that as the crystallizer inner diameter increased, the elongation and impact energy decreased in both states.
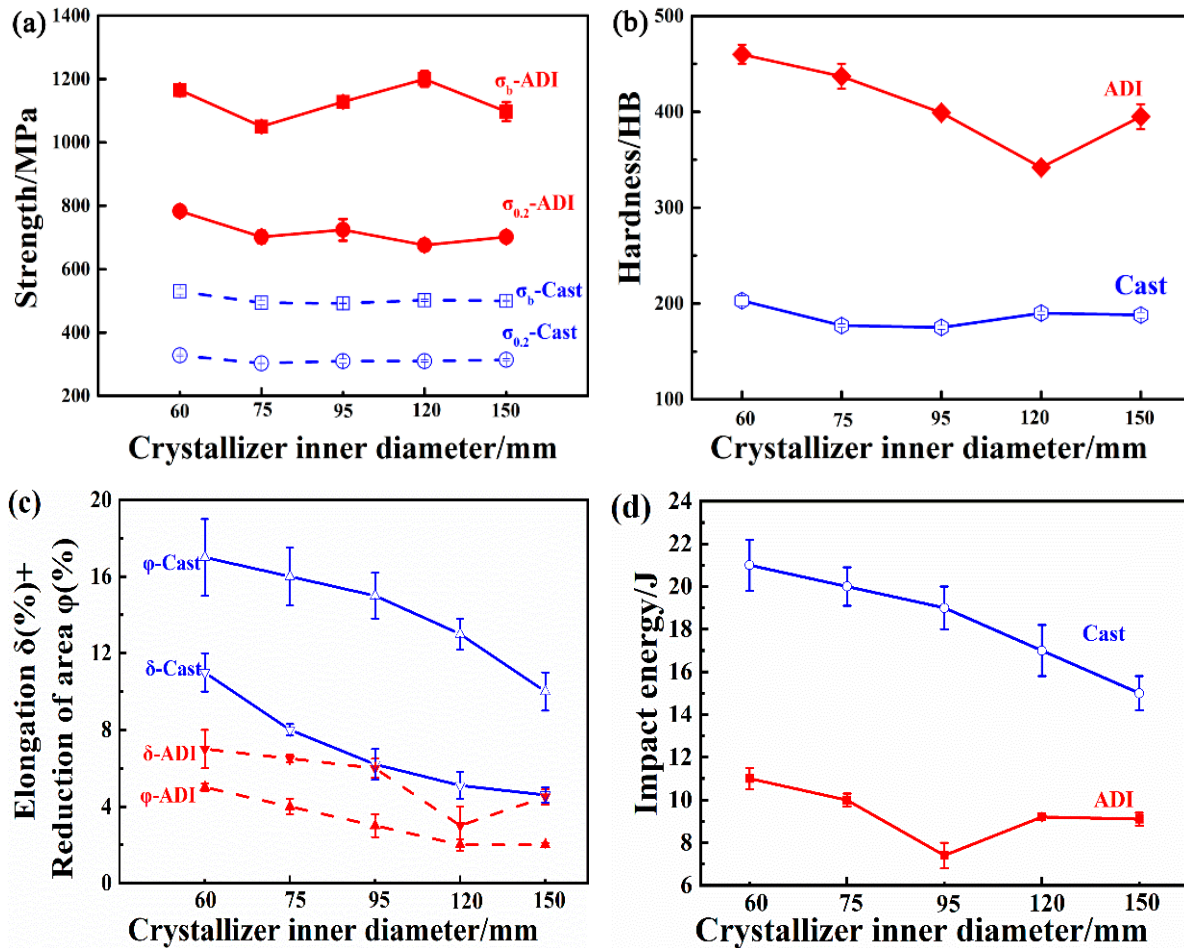

Figure 6. Mechanical properties of different as-cast ductile iron and ADI state specimen: (**a**) strength; (**b**) hardness; (**c**) elongation and the reduction of area; (**d**) impact energy.

4. Discussion

Javaid et al. [24] reported that samples with lower-diameter crystallizers had a significantly stronger tensile and yield strength because of a more homogeneous microstructure, a higher nodule number, and a better graphite nodularity rate. A smaller crystallizer inner diameter yields a larger supercooling, a finer pearlite spacing, and smaller ferrite particles [25,26]. A pearlite content for the AC 60 specimen shows a smaller difference from that for the AC 150 sample, but σ_b and $\sigma_{0.2}$ are higher than that of the AC 150 samples. In the AC 95, the pearlite volume content is 17.6%, which is almost half of that for the AC 150 (33.4%). Pearlite is strong, but σ_b and $\sigma_{0.2}$ of AC 95 and AC 150 show little difference. The AC 60 specimen has a nodular graphite diameter class of 8, with a nodularity rate of 100% which is the highest. The nodular graphite is distributed uniformly in the matrix. The number of nodular graphite decreases for the AC 150 specimen. When the nodular graphite diameter class is 6, the nodularity rate decreases to 70%, and chunks of graphite are produced, which appear to be small graphite scraps that are dispersed in the matrix. The emergence of chunky graphite decreases the tensile strength, the elongation, and the area reduction [27,28]. The higher nodularity rate of graphite in ductile iron does not cause an obvious stress concentration, which therefore results in a significant improvement of the

strength, plasticity, and toughness [29]. The improvement in graphite nodularity rate is an important way to improve the ductile iron properties.

The mechanical properties of ADI are affected by several factors. The tensile and yield strength of materials are related to the content and morphology of bainitic ferrite, whereas the toughness is related to the V_γ and the C_γ. A more irregular bainitic ferrite distribution yields a more disordered orientation, a larger interface energy and higher tensile strength, yield strength and hardness. The C_γ and the V_γ should be as high as possible to improve the impact toughness [17].

The as-cast specimens after austempering have higher tensile strength and yield strength but show a decrease in elongation. Figure 5 shows the ADI microstructures and the XRD analysis diagram. The results show that with an increase in crystallizer inner diameter, the overall V_γ increases, the bainitic ferrite content decreases initially and then increases, with an overall decrease. For the ADI 60, the bainitic ferrite particles are small with a maximum interfacial area, and the largest transition kinetics. After austempering, the highest content of acicular bainite ferrite and the lowest γ_{hc} content is obtained. For the ADI 75, 95, 120, and 150 samples, the C_γ is higher than that in the ADI 60 specimen, the bainitic ferrite is lower, and the strength, hardness, and impact toughness of the ADI 60 specimen are higher than that of the ADI 75-, 95-, 120-, and 150 samples. Because the toughness and strength of fine acicular bainite ferrite are better than that of coarse bainite ferrite, and the nodular graphite is distributed uniformly in the crystallizer with an inner diameter of 60 mm, the nodular graphite and the stress concentration are small, the cutting and reducing effect of the matrix is reduced, therefore, the mechanical property of the ADI 60 sample is the best. A comparison of the effect of nodular graphite on the properties of the as-cast specimens shows that the influence of nodular graphite remains the same. In the ADI 75 and ADI 95 samples with different graphite nodule numbers, the diameter class and nodularity rate of the nodular graphite are the same. With an increase in crystallizer inner diameter, the V_γ increases and the acicular bainite orientation tended to be straight and parallel. Compared with the ADI 120 sample, the ADI 150 sample shows an increase in the residual austenite content, a decrease in the nodularity rate and the amount of nodular graphite, and the presence of chunky graphite brings poor mechanical properties.

In this study, because of the crystallizer inner diameter difference, different original as-cast microstructures and ADI microstructures are obtained, under the same isothermal quenching condition. The initial as-cast microstructure affects the microstructures and properties of the austempered ductile iron obtained after isothermal quenching. Ferrite has a low carbon content, pearlite has a high carbon content, and the graphite has the highest carbon content. Because of the different carbon contents of the initial structure, when the temperature increases, the material transforms into austenite with different carbon contents, which results in carbon-rich and carbon-poor areas in austenite and promotes carbon diffusion [30]. An increased number of phase interfaces yields a better austenite nucleation. In the as-cast initial structure with a crystallizer inner diameter of 60 mm, the ferrite particles are small, the pearlite layer spacing is small, the number of nodular graphite per unit area is the largest, and the diffusion distances for carbon are shorter in the grain-refined microstructure, which facilitates carbon partitioning. When the temperature increased to the austenitization temperature, more phase interfaces are favorable for austenite nucleation. Hillert et al. [31] has reported that the process of forming austenite from pearlite is controlled by carbon diffusion and that the effective distance of diffusion is approximately equal to the interlamellar spacing of pearlite. The finer pearlite will provide more nucleation sites for austenite formation. The refined austenite microstructure provides more nucleation sites for bainite and the process of ferrite formation is rapid, which refines the bainite packet structure [32]. For the larger crystallizers, the nodular graphite micro structure gets coarser, as well as the bainite microstructure after austempering heat-treatment. After austempering, bainite ferrites with different morphologies and different contents form with a high austenite carbon

content, and determine the mechanical properties of the ADI. This study gives a qualitative investigation of the relationship between heterogeneous microstructure [33] and mechanical properties, and the detailed and systematic investigations are for the future investigation, which may include advanced characterization methods such as in situ mechanical testing in microscopes [34,35].

Different crystallizer inner diameters correspond to different as-cast microstructures and yield different ADI microstructures under the same austempering conditions, as well as the morphology of bainite ferrite, the volume fraction of high-carbon austenite, and the carbon content in austenite. With the increasing crystallizer inner diameter, the cooling speed of casting decreases, the number of nodular graphite decreases, the spacing between nodular graphite increases, and sometimes chunky graphite appears, which reduces the toughness. In this work, the similar microstructure as the traditional isothermal quenching is obtained after the isothermal quenching of specimens from different-inner-diameter casting crystallizers, but with different mechanical properties. Different crystallizer inner diameters can be selected according to different mechanical property requirements.

5. Conclusions

Different original as-cast microstructures from crystallizers with different inner diameters under the same austempering process, yields austempered ductile cast iron with different mechanical properties. By comparing the microstructures and mechanical properties in the two states, the following conclusions are made:

(1) Nodular graphite is mainly determined by casting crystallizer but not the subsequent heat treatment. It is revealed that with an increase in the casting crystallizer inner diameter, the amount of nodular graphite decreases and the nodular graphite diameter increases. Different crystallizer inner diameters correspond to different as-cast microstructures and yield different ADI microstructures under the same austempering conditions, but have little effect on the morphology and amount of nodular graphite during the heat treatment process.

(2) Phase volume fractions are affected by the casting crystallizer in both the as-cast ductile iron and ADI. With an increase in the casting crystallizer inner diameter, the pearlite content decreases initially and then increases, but the ferrite shows the opposite trend. After the same austempering process, with the increase in the crystallizer inner diameter, the carbon content of austenite increases initially then decreases, and the acicular ferrite morphology changes from disordered to regular, from fine to coarse.

(3) Mechanical properties are affected by characters of nodular graphite both in the as-cast ductile iron and ADI. The diameter, shape, and distribution uniformity of nodular graphite influence the ductility of the as-cast ductile iron and ADI. The smaller nodular graphite particles yield a more homogeneous distribution and a better ductility. The higher disordered acicular ferrite content yields a higher tensile strength, a higher austenite content, and higher carbon content in the austenite, with a higher toughness.

(4) Heat treatment of austenite results in strong effects on mechanical properties. It is revealed that the strength of the cast iron increases by 120% and the hardness increases by 140%, through the austempering treatment. Smaller graphite introduces less stress concentration. Chunky graphite reduces the toughness and a reasonable casting crystallizer inner diameter can be chosen according to different mechanical property requirements.

Author Contributions: Conceptualization, J.B., X.C. and W.C.; Methodology, J.B. and Y.X.; software, J.B.; validation, H.X.; Formal analysis, J.B.; investigation, J.B. and W.C.; resources, W.C.; Data curation, J.B., H.X., Y.W., X.C. and X.Z.; Writing—original draft, J.B.; Writing—review and editing, X.C. and W.C.; Supervision, Y.W.; project administration, J.B. and X.C.; funding acquisition, X.C. All authors have read and agreed to the published version of the manuscript."

Institutional Review Board Statement: Not applicable.

Informed Consent Statement: Not applicable.

Data Availability Statement: The data presented in this study are available on request from the corresponding author.

Conflicts of Interest: The authors declare no conflict of interest.

References

1. Ghasemi, R.; Elmquist, L.; Svensson, H.; König, M.; Jarfors, A.E.W. Mechanical properties of Solid Solution-Strengthened CGI. *Int. J. Cast Met. Res.* **2016**, *29*, 98–105. [CrossRef]
2. Li, X.H.; Saal, P.; Gan, W.M.; Hoelzel, M.; Volk, W.; Petry, W.; Hofmann, M. Strain-Induced Martensitic Transformation Kinetic in Austempered Ductile Iron (ADI). *Met. Mater. Trans. A* **2017**, *49*, 94–104. [CrossRef]
3. Kasvayee, K.A.; Ghassemali, E.; Svensson, I.L.; Olofsson, J.; Jarfors, A.E. Characterization and modeling of the mechanical behavior of high silicon ductile iron. *Mater. Sci. Eng. A* **2017**, *708*, 159–170. [CrossRef]
4. Melado, A.C.; Nishikawa, A.; Goldenstein, H.; Giles, M.; Reed, P. Effect of microstructure on fatigue behaviour of advanced high strength ductile cast iron produced by quenching and partitioning process. *Int. J. Fatigue* **2017**, *104*, 397–407. [CrossRef]
5. Panneerselvam, S.; Putatunda, S.K.; Gundlach, R.; Boileau, J. Influence of intercritical austempering on the microstructure and mechanical properties of austempered ductile cast iron (ADI). *Mater. Sci. Eng. A* **2017**, *694*, 72–80. [CrossRef]
6. Alabbasian, F.; Boutorabi, S.M.A.; Kheirandish, S. Effect of inoculation and casting modulus on the microstructure and mechanical properties of ductile Ni-resist cast iron. *Mater. Sci. Eng. A* **2016**, *651*, 467–473. [CrossRef]
7. Vicente, A.D.A.; Moreno, J.R.S.; Santos, T.F.D.A.; Espinosa, D.C.R.; Tenório, J.A.S. Nucleation and growth of graphite particles in ductile cast iron. *J. Alloys Compd.* **2019**, *775*, 1230–1234. [CrossRef]
8. Liu, Y.; Li, Y.; Xing, J.; Wang, S.; Zheng, B.; Tao, D.; Li, W. Effect of graphite morphology on the tensile strength and thermal conductivity of cast iron. *Mater. Charact.* **2018**, *144*, 155–165. [CrossRef]
9. Zhang, H.; Wu, Y.; Li, Q.; Hong, X. Mechanical properties and rolling-sliding wear performance of dual phase austempered ductile iron as potential metro wheel material. *Wear* **2018**, *406-407*, 156–165. [CrossRef]
10. Yang, J.; Putatunda, S.K. Near threshold fatigue crack growth behavior of austempered ductile cast iron (ADI) processed by a novel two-step austempering process. *Mater. Sci. Eng. A* **2005**, *393*, 254–268. [CrossRef]
11. Rao, P.P.; Putatunda, S.K. Influence of microstructure on fracture toughness of austempered ductile iron. *Metall. Mater. Trans. A* **1997**, *28*, 1457–1470. [CrossRef]
12. Putatunda, S.K.; Kesani, S.; Tackett, R.; Lawes, G. Development of austenite free ADI (austempered ductile cast iron). *Mater. Sci. Eng. A* **2006**, *435*, 112–122. [CrossRef]
13. Bartosiewicz, L.; Krause, A.R.; Kovacs, B.; Putatunda, S.K. Fatigue crack growth behavior of austempered ductile cast iron. *AFS Trans.* **1992**, *92*, 135–142.
14. Petersen, L.R.; Putatunda, S.; Singh, I. Fracture Toughness of Unalloyed Austempered Ductile Cast Iron (ADI). *J. Test. Eval.* **1995**, *23*, 325. [CrossRef]
15. Aranzabal, J.; Gutierrez, I.; Rodriguez-Ibabe, J.M.; Urcola, J.J. Influence of the amount and morphology of retained austenite on the mechanical properties of an austempered ductile iron. *Met. Mater. Trans. A* **1997**, *28*, 1143–1156. [CrossRef]
16. Panneerselvam, S.; Martis, C.J.; Putatunda, S.K.; Boileau, J.M. An investigation on the stability in Austempered Ductile Cast Iron (ADI). *Mater. Sci. Eng. A* **2015**, *28*, 237–246. [CrossRef]
17. Upadhyaya, R.; Singh, K.K.; Kumar, R.; Chandran, M.S. Study on The Effect Of Austempering Temperature On The Structure-Properties Of Thin Wall Austempered Ductile Iron. *Mater. Today Proc.* **2018**, *5*, 13472–13477. [CrossRef]
18. Bendikiene, R.; Ciuplys, A.; Cesnavicius, R.; Jutas, A.; Bahdanovich, A.; Marmysh, D.; Nasan, A.; Shemet, L.; Sherbakov, S. Influence of Austempering Temperatures on the Microstructure and Mechanical Properties of Austempered Ductile Cast Iron. *Metal* **2021**, *11*, 967. [CrossRef]
19. Borsato, T.; Ferro, P.; Berto, F.; Carollo, C. Fatigue strength improvement of heavy-section pearlitic ductile iron castings by in-mould inoculation treatment. *Int. J. Fatigue* **2017**, *102*, 221–227. [CrossRef]
20. Zhang, X.; Liu, W.; Godfrey, A.; Liu, Q. The Effect of Long-Time Austenization on the Wear Resistance and Thermal Fatigue Properties of a High-Speed Steel Roll. *Met. Mater. Trans. A* **2009**, *40*, 2171–2177. [CrossRef]

21. *ASTM E-8*; Standard Test Method for Tensile Testing of Metallic Materials. ASTM International: West Conshohocken, PA, USA, 1997.

22. Górny, M.; Tyrała, E. Effect of Cooling Rate on Microstructure and Mechanical Properties of Thin-Walled Ductile Iron Castings. *J. Mater. Eng. Perform.* **2012**, *22*, 300–305. [CrossRef]

23. Song, L.; Guo, E.; Wang, L.; Liu, D. Effects of Silicon on Mechanical Properties and Fracture Toughness of Heavy-Section Ductile Cast Iron. *Metals* **2015**, *5*, 150–161. [CrossRef]

24. Javaid, A.; Thomson, J.; Davis, K.G.; Sahoo, M. Effect of Microstructure on the Mechanical Properties of Thin-Wall Ductile Iron Castings. *Am. Foun. Soc.* **2001**, *109*, 1–18.

25. Zhang, X.; Hansen, N.; Godfrey, A.; Huang, X. Structure and strength of sub-100 nm lamellar structures in cold-drawn pearlitic steel wire. *Mater. Sci. Technol.* **2017**, *34*, 794–808. [CrossRef]

26. Nikas, D.; Zhang, X.; Ahlström, J. Evaluation of local strength via microstructural quantification in a pearlitic rail steel deformed by simultaneous compression and torsion. *Mater. Sci. Eng. A* **2018**, *737*, 341–347. [CrossRef]

27. González-Martínez, R.; De la Torre, U.; Ebel, A.; Lacaze, J.; Sertucha, J. Effects of high silicon contents on graphite morphology and room temperature mechanical properties of as-cast ferritic ductile cast irons. Part II–Mechanical properties. *Mat. Sci. Eng. A* **2017**, *712*, 794–802. [CrossRef]

28. Benedetti, M.; Torresani, E.; Fontanari, V.; Lusuardi, D. Fatigue and Fracture Resistance of Heavy-Section Ferritic Ductile Cast Iron. *Metals* **2017**, *7*, 88. [CrossRef]

29. Chen, S.-L.; Hu, J.; Zhang, X.-D.; Dong, H.; Cao, W.-Q. High Ductility and Toughness of a Micro-duplex Medium-Mn Steel in a Large Temperature Range from −196 °C to 200 °C. *J. Iron Steel Res. Int.* **2015**, *22*, 1126–1130. [CrossRef]

30. Wu, Y.S. The influence of original microstructure on the structure and mechanical properties of ADI. *China Foundry* **1998**, *3*, 18–22.

31. Hillert, M. On the theory of normal and abnormal grain growth. *Acta Metall.* **1965**, *13*, 227–238. [CrossRef]

32. Wang, C.; Du, X.; Li, S.; Sun, Y.; Yang, P. Morphology and Crystallography of Ausferrite in Austempered Ductile Iron. *Metal* **2017**, *7*, 238. [CrossRef]

33. Zhang, X.; Nielsen, C.V.; Hansen, N.; Silva, C.; Martins, P.A. Local stress and strain in heterogeneously deformed aluminum: A comparison analysis by microhardness, electron microscopy and finite element modelling. *Int. J. Plast.* **2019**, *115*, 93–110. [CrossRef]

34. Pan, H.; He, Y.; Zhang, X. Interactions between Dislocations and Boundaries during Deformation. *Materials* **2021**, *14*, 1012. [CrossRef] [PubMed]

35. Zhang, X.; Godfrey, A.; Winther, G.; Hansen, N.; Huang, X. Plastic deformation of submicron-sized crystals studied by in-situ Kikuchi diffraction and dislocation imaging. *Mater. Charact.* **2012**, *70*, 21–27. [CrossRef]